Iraqi Journal of Physics, 2025
https://doi.org/10.30723/ijp.v23i3.1383

Vol. 23, No.3, PP. 24-39
P-ISSN: 2070-4003
E-ISSN: 2664-5548

Investigating the Nuclear Structure of ^{65}Cu using the Shell Model and Hartree-Fock+BCS Approach

Ruwaida T. Mahdi[1*] and Ali A. Alzubadi[2]
[1]*Department of Physics, College of Science for Women, University of Baghdad, Baghdad, Iraq*
[2]*Department of Physics, College of Science, University of Baghdad, Baghdad, Iraq*
[*]Corresponding author: ruwaida.tareq1104a@sc.uobaghdad.edu.iq

Ali A. Alzubadi is a journal editor, but he participated only as an author in the peer review process. The authors declare no other conflicts of interest

Abstract

This research studied the nuclear deformation of the ^{65}Cu isotope by employing advanced shell model calculations alongside the Hartree-Fock approximation within the framework of the *fp*-shell model space. A detailed analysis of inelastic electron scattering was conducted, focusing on both the longitudinal and transverse form factors, as well as excitation energies. These calculations were performed using the shell model, incorporating elements of the one-body transition density matrix and leveraging the full *fp*-shell space to facilitate the JUN45 interaction. Various theoretical wave functions, including the harmonic oscillator (HO), Skyrme Hartree-Fock (SLy4), and Wood-Saxon (WS) potentials, were applied, and their results were meticulously compared with experimental data. Furthermore, the potential energy surfaces were explored as a function of quadrupole deformation parameters through the SLy5 parameterization within the Hartree-Fock approach. Notably, the shell model computations were executed using the NushellX@MSU code without imposing any constraints on the model space, offering a comprehensive and unconstrained insight into the nuclear structure dynamics of ^{65}Cu. Finally, the calculated results were compared with the available experimental data.

Article Info.

Keywords:
fp-Shell Model, Skyrme Hartree-Fock, Quadrupole Deformation, Form Factors, Excitation Energies.

Article history:
Received: Oct. 13, 2024
Revised: Nov. 06, 2024
Accepted:Nov. 23, 2024
Published:Sep. 01,2025

1. Introduction

There are three essential regards to the shell model (SM) approach to nuclear structures: the valence space, the effective interaction, and the computational tools that enable the solution of the massive issues involved [1]. The main concept is that protons and neutrons in a nucleus are in motion within a mean field (MF) that is generated self-consistently. The MF can be estimated using Wood-Saxon (WS) or harmonic oscillator (HO) potentials as long as a significant spin-orbit aspect is included. By adding the latter, the single-particle energy spectrum shows a shell structure that accounts for the experimentally observed magic numbers of protons and neutrons [2,3]. Most nuclei have a flat structure, where a small number of valence particles interact with an inert core through the residual nuclear force, leading to a relatively even distribution of particle density (protons and neutrons) throughout the nucleus without a significant decrease from the center to the edges. It was initially believed that this interaction and residual force originated from the fundamental interplay of free protons and neutrons [4,5].

The spherical shell model can handle many nuclear excitations concurrently, including rotational bands from well-deformed intrinsic states, single-particle modes, neutron-neutron and proton-neutron pairing correlations. The pairing interactions between protons, neutrons, and neutrons affect the stability of the nucleus through the bonds between the particles, which contribute to their distribution within the nucleus [6-9]. A unified model that can predict the structure and features of nuclei has been sought

© 2025 The Author(s). Published by College of Science, University of Baghdad. This is an open-access article distributed under the terms of the Creative Commons Attribution 4.0 International License (https://creativecommons.org/licenses/by/4.0/).

by scientists for some time [10-13]. Since nuclear physics was discovered, theoretical studies have so focused on nuclei and their structures and behaviours ever.

Theoretical frameworks and approaches ranging from basic answers and conjectures to more complicated models have been devised to account for experimental findings. Light nuclei, defined as nuclei with a mass number A < 50, may be modelled using the bare N-N interaction [14, 15]. The use of SM is possible for nuclei with middle mass numbers [16–18]. Nevertheless, relativistic [19] and nonrelativistic [20, 21] MF theory can be applicable to heavy nuclei (nuclei with A > 60). The Hartree –Fock HF model, incorporating BCS theory, is the most favored model, considering pairing correlations with MF and being popular among all other models[22,23].

Our goal was to study the form factors for inelastic longitudinal and transverse electron scattering for ^{65}Cu nuclei in the *fp*-shell region. The effective JUN45 [24] interaction was utilized in performing SM calculations for the *jj44* model space. The SM calculation was carried out using the NushellX@MSU code without any constraints on the model space [25]. Also, the potential energy curves as a function of the quadrupole deformation parameters were studied using the HF calculations with SLy5 parameterization. The structure of this paper is as follows: Section 2 briefly introduces the SM and HF Method, while section 3 covers the presentation of results and discussions. In section 4, the study conclusions.

2. Theoretical Framework

This section describes two types of formalism for calculations that uses the SM calculations and HF approximation.

2.1. Shell Model Calculations

When the components of the single-particle matrix and the One-Body transition Density Matrix (OBDM) are added together, the nuclear matrix element of the electromagnetic ($\hat{o}$) operator is [26]

$$\langle f \| \hat{o}\,(\lambda)_{t_z} \| i \rangle \quad = \sum_{k_a k_b} OBDM(f i k_a k_b \lambda)\, \langle k_a \| \hat{o}\,(\lambda)_{t_z} \| k_b \rangle \tag{1}$$

where $\hat{X}$ operator stands for $\hat{O}$ operator for electromagnetic. The *OBDM* is given by

$$OBDM(f i k_a k_b \lambda) = \frac{\langle f \| a^{+}_{ka} \otimes \tilde{a}_{\mathrm{kb}} \| i \rangle}{\sqrt{2\lambda + 1}} \tag{2}$$

All of the necessary quantum numbers to differentiate between the states are present in both I and f. The nuclear magnetic dipole moment is described by the M

$$\mu_{Th} = \sqrt{\frac{4\pi}{3}} \begin{pmatrix} \mathrm{J} & 1 & \mathrm{J} \\ -\mathrm{J} & 0 & \mathrm{J} \end{pmatrix} \sum_{t_z} \langle f \| \hat{O}\,(M1)_{t_z} \| i \rangle_{\mu_N} \tag{3}$$

The nuclear magnetic is represented by $\mu_N = \frac{eh}{2m_p c} = 0.1051\ efm$. In relation to the E2 operator, the electric quadrupole moment is defined as

$$Q_{Th} = \sqrt{\frac{16\pi}{5}} \begin{pmatrix} \mathrm{J} & 2 & \mathrm{J} \\ -\mathrm{J} & 0 & \mathrm{J} \end{pmatrix} \sum_{t_z} \langle f \| \hat{O}\,(E2)_{t_z} \| i \rangle e_{t_z} \tag{4}$$

The initial and final nuclear many body states include all the necessary quantum numbers to differentiate between nuclear states $| J \rangle$. The Skyrme potential, a two-body interaction, is used by the central potential. It may be converted into a single-body potential in the HF approximation. It is a potential that represents the average effect of all nucleons in the nucleus, taking into account both two-body and three-body nucleon interactions. The Skyrme potential V_{Skyrme} can be written as [27]

$$V_{Skyrme}(\vec{r}_1, \vec{r}_2) = t_0(1 + x_0 \hat{p}_\sigma)\delta_{12} + \frac{t_1}{2}(1 + x_1 \hat{p}_\sigma)\left[\vec{k}'^2 \delta_{12} + \vec{k}^2 \delta_{12}\right]$$

$$+t_2(1+x_2\hat{p}_\sigma)k'\delta_{12}k+\frac{t_3}{6}(1+x_3\hat{p}_\sigma)p^{\alpha}\left(\frac{\vec{r}_1-\vec{r}_2}{2}\right)\delta_{12}+iW_0\vec{k}'\delta_{12}(\hat{\vec{\sigma}}_1+\hat{\vec{\sigma}}_2)\times\vec{k}$$

$$+\frac{t_e}{2}\left(\left[3(\hat{\vec{\sigma}}_1.\vec{k}')(\hat{\vec{\sigma}}_2.\vec{k}')-(\hat{\vec{\sigma}}_1.\hat{\vec{\sigma}}_2)\vec{k}'^2\right]+\delta_{12}\left[3(\hat{\vec{\sigma}}_1.\vec{k})(\hat{\vec{\sigma}}_2.\vec{k})-(\hat{\vec{\sigma}}_1.\hat{\vec{\sigma}}_2)\vec{k}^2\right]\right)$$

$$+t_0\left[3(\hat{\vec{\sigma}}_1.\vec{k})\delta_{12}(\hat{\vec{\sigma}}_2.\vec{k}')-(\hat{\vec{\sigma}}_1.\hat{\vec{\sigma}}_2)\vec{k}'\delta_{12}\vec{k}'\right] \quad \textbf{(5)}$$

where $\delta_{12} = \delta(\vec{r}_1-\vec{r}_2)$ and k, k' are the relative momentum operators with k acting on the right, and k' acting on the left and are given by

$$\hat{k}=\frac{1}{2i}\left(\vec{\nabla}_1-\vec{\nabla}_2\right) \quad , \quad \hat{k}'=\frac{1}{2i}\left(\vec{\nabla}_1-\vec{\nabla}_2\ \right) \quad \textbf{(6)}$$

$\hat{P}_\sigma$ is the spin-exchange operator that is given as:

$$\hat{P}_\sigma=\frac{1}{2}(1+\vec{\sigma}_1.\vec{\sigma}_2) \quad (7)$$

$\hat{\sigma}$ is the spin operator.

F(C λ , q, f, i) is the longitudinal Coulomb form factor, F(E λ, q, f, i) is the transverse electric one, and F(M λ , q, f, i) is the transverse magnetic one, where λ is the multipolarity [28]. Convection currents λ_c, created by the orbital movement of nucleons, and magnetization currents λ_m, caused by the magnetic moments of the nucleons, may be used to classify the last two form factors. Therefore, it is possible to describe the entire longitudinal form factor as

$$|F_C(q,f,i)|^2=\sum\nolimits_{\lambda\geq 0}|F(C\,\lambda\,,q,f,i)|^2 \quad \textbf{(8)}$$

and the total transverse form factor as

$$|F_T(q,f,i)|^2=\sum\nolimits_{\lambda>0}\ \{|F(E\,\lambda\,,q,f,i)|^2+|F(M\,\lambda\,,q,f,i)|^2\} \quad \textbf{(9)}$$

By including the rotational momentum l and the momentum transfer q, which link the initial (i) and final (f) states in the nuclear shell model, the form factor for electroexcitation may be given as [29]

$$|\,F(\eta\lambda,q)|^2=\frac{4\pi}{Z^2(2J_i+1)}\left|\langle f\|\hat{T}\ (\eta\lambda,q)\|i\rangle\,F_{c.m}\ (q)F_{f.s}\ (q)\right|^2 \quad \textbf{(10)}$$

where η stands for the Coulomb C longitudinal and transverse form factors. In the SM, the finite size (f.s.) nucleon form factor superscript compensates for the lack of translational invariance; A represents the mass number, while b represents the size parameter of the harmonic oscillator (HO).

2.2. Hartree –Fock + Bardden-Cooper- Schriefer Calculations

The self-consistent mean field approach examines nuclear structure and shape development by integrating HF and BCS computations. Density shape changes, taking pairing correlations into account, are studied using skyrme forces, abbreviated as SHF. When trying to forecast the group binding energies and individual energy levels of closed-shell nuclei, the HF technique is probably the best bet [30]. In addition, SHF's zero-range interactions and central character make it useful [31, 32]. Nuclei are a many-body system in quantum mechanics that show quadrupole collectivity linked to the mean field's shape. The measure of operator $\hat{Q}$ is linked to the overall degree of freedom. A mean-field theory is constructed from individual wave functions ψα and fractional occupation amplitudes υα [33], i.e. $\{\varphi_{\alpha,}v_\alpha,\alpha=1,\dots,\Omega\ \}$.

In the active single-particle space, Ω represents the size while the occupation amplitudes are constrained within the range 0 ≤ υα ≤ 1. The BCS many-body state is constructed from these elements, resulting in the comple mentary non-occupation amplitude [33]

$$|\phi\rangle = \prod_{\alpha>0}(u_\alpha + v_\alpha \hat{a}_\alpha^+ \hat{a}_{\bar{\alpha}}^+)|0\rangle \tag{11}$$

$|0\rangle$ represents the particle-vacuum state, $\hat{a}_\alpha^+$ is the creation operator for a Fermion in the state $\psi\alpha$, and $\bar{\alpha}$ is the time reversed partner of state α. The density of nucleons in the vicinity is defined as [24]

$$\rho_q(\vec{r}) = \sum_{\alpha\in q}\sum_s v_\alpha^2\ |\psi_\alpha(\vec{r}, s)|^2 \tag{12}$$

The total energy is composed as

$$E_{tot} = T + E_{Skyrme} + E_{Coulomb} + E_{pair} + E_{cm} \tag{13}$$

E_{Skyrme} :Skyrme energy, E_{Culomb} : Coulomb energy

$$E_C = \frac{e^2}{2}\int dV dV' \frac{\rho_p(\vec{r})\rho_p(\vec{r}')}{|\vec{r}-\vec{r}|} - \int dV \frac{3e^2}{4}\left(\frac{3}{\pi}\right)^{\frac{1}{3}} \rho_p^{4/3} \tag{14}$$

and the pairing energy is

$$E_{pair} = \frac{1}{4}\ \sum_{q\epsilon\{p,n\}} V_{pair,q}\int dV\left|\xi_q\right|^2\left[1-\frac{\rho}{\rho_{0,pair}}\right] \tag{15}$$

In complete three-dimensional space, dV represents the volume element, e represents the elementary charge with e^2 equaling 1.43989 MeV.fm, and ξ_q is the pairing density [33].

$$\xi_q = \sum_{\alpha\in q}\sum_s w_\alpha\ u_\alpha\ v_\alpha\,\psi_{\bar{\alpha}}(\vec{r}, s)\psi_\alpha(\vec{r}, s) \tag{16}$$

w_α indicates a rather small boundary of the pairing region. In the wave functions, the spinor component is denoted by the variables s $\epsilon \pm 1$. Volume and surface pairing equilibrium is affected by the pairing energy parameter ρ_0. To put it simply, nuclear deformation occurs when the electric quadrupole moment shows that the nucleus is not exactly symmetrical around its centre of mass. Accordingly, the times of centre of mass are the key moments [33]

$$\vec{R}_{type} = \frac{\int dV\vec{r}\,\rho_{type}(\vec{r})}{\int dV\rho_{type}(\vec{r})} \tag{17}$$

Any of the following may be considered a "type": an isovector moment from the isovector density, an isoscalar or total from the total density $\rho = \rho_p + \rho_n$, a proton from ρ_p, or a neutron from ρ_n.

$$\rho_{T=1} = (A)\,\rho_p - (Z/A)\,\rho_n \tag{18}$$

The anisotropic mixtures can be measured using the spherical quadrupole moments [33].

$$Q_{2m,type} = \int dVr^2 Y_{2m}\,\rho_{type}(\vec{r} - \vec{R}_{type}) \tag{19}$$

Only at m=0 can non-zero quadrupole moments be accommodated by the existence of axial symmetry. In many cases, it is more practical to express them as a quadrupole deformation parameter, which is a dimensionless quadrupole moment

$$\beta_{20} = \frac{4\pi}{3}\frac{Q_{20}}{AR^2} \quad ,R = R_0A^{1/3}\ ,R_0 = 1.2\,fm \tag{20}$$

In axial coordinate-space, wave functions and fields coexist on a grid. The article delves into the topic of axial coordinates and its relationship to Cartesian coordinates [33].

$$r = \sqrt{X^2 + Y^2}\,, Z = Z \tag{21}$$

R represents the axial coordinate that shows the space point's distance from the symmetry axis. Symmetrical objects, such as densities and potentials, are based solely on the r and z coordinates, which are both illustrated on a uniform grid

$$r \leftrightarrow \{r_0, \dots, r_{N_r}\}, r_v = v\Delta r \tag{22}$$

$$z \leftrightarrow \{(z_{-N_z} \dots, z_{-1}), z_0, \dots, z_{N_z}\}, z_v = v\Delta z \tag{23}$$

The variables Δr and Δz stand for the grid spacing's numerical parameters. The grid is filled along the z-axis from 0 to +Nz using reflection symmetry to rebuild the complete grid, or from -Nz to +Nz, allowing for reflection-asymmetric nuclear topologies. The axially symmetric functions f (r,z) that represent potentials and densities may be simply written as $f\,(r_{vr}, z_{vz})$ on the grid. The angular dependence and spin make a single particle wave function more complex. It is shown as [33]

$$\psi_\alpha = \begin{pmatrix} \psi_\alpha^{(+)}\,(r_{v_r}, z_{v_z})\exp\,(i m_\alpha\,\phi) \\ \psi_\alpha^{(-)}\,(r_{v_r}, z_{v_z})\exp\,(i(m_\alpha\,+1)\phi) \end{pmatrix} \tag{24}$$

In the upper spin component, the z-component of the orbital angular momentum is denoted by m_α, and the z-component of the total z angular momentum is $k_\alpha = m_\alpha + 1/2$.

3. Results and Discussions

Our current study utilized the most recent NuSellX@MSU code [24] to compute the OBDM elements in the full *fp*-shell model space. This space includes the $1f_{7/2}$, $2p_{3/2}$, $1f_{5/2}$ and $2p_{1/2}$ valence orbitals with a ^{40}Ca nucleus serving as the inert core *JUN45* effective interaction. Additionally, the HF+BCS code was employed to analyze the β_2 as a function of energy. Our discussion of the results was divided into four sections: the first section focuses on electroexcitation form factors, followed by excitation energies, and finally, the β_2 parameter was explored using the HF +BCS method.

3.1 Inelastic Electron Scattering Form Factors

The study of inelastic electroexcitation form factors gives a full and detailed investigation of electromagnetic properties and the internal structure of the nuclei [33, 34]. This study takes into consideration quite a wide range of nuclear processes. It applies different nuclear single-particle models, such as Skyrme-Hartree Fock (SLy4) [30], harmonic oscillator (HO) [28] and Woods- Saxon (WS) [29]. Having performed such a comparison for Cu isotope, the validity of the models was confirmed, and what can be done to enhance them was indicated. In most cases studied, the shell-model version of the Bohr-Mottelson (BM) collective model was employed. This version utilizes microscopic collective models to derive the collective (rotational and vibrational) modes from the Schrödinger equation for the many-particle nuclear Hamiltonian, in contrast to the postulated modes in the phenomenological collective models.

The effective charges were formulated following BM [3] to explicitly include neutron excess and generally compensate for missing excitations beyond the limited model space via the relations $e_n^{BM} = e_{pol}$ and $e_p^{BM} = 1 + e_{pol}$ where the e_{pol} term is given by the following equation $e_{pol} = e\{Z/A - 0.32(N-Z)/A + [0.32 - 0.3(N-Z)/A]\tau_z\}$.

3.1.1 Longitudinal C2 form factors

Fig. 1 presents the calculated C2 form factors for the excited states $1/2_1$, $1/2_2$, Fig.2 presents those for $5/2_1$, $5/2_2$, and Fig. 3 for $7/2_1$, and compared with experimental data from the work of Erler et al. [35], covering a momentum transfer range of q=0 - 2.8 fm^{-1}. The C2 form factors for the $1/2_1$ state (0.771 MeV) and $1/2_2$ state (2.212 MeV) are shown in Figs. (1a) and (1b), respectively.

In Fig. (1a), the C2 form factors calculated using the SLy4, HO, and WS showed good agreement with the experimental data, particularly at the first and second maxima. In contrast, the calculated data overestimated the experimental in Fig. (1b).

Figs. (2a) and (2b) display the C2 form factors for the $5/2_1$ state (1.115 MeV) and $5/2_2$ state (1.623 MeV). In Fig.(2a), the Tassie model calculations [35] showed enhancement at the first, second, and third maxima, aligning well with the experimental data. However, in Fig. (2b), the calculated C2 form factors underestimated the experimental data across all momentum transfer regions.

Finally, Fig. 3 presents the C2 form factor for the $7/2_1$ state (1.481 MeV), where the Tassie model calculations accurately described the experimental data across all q-values.

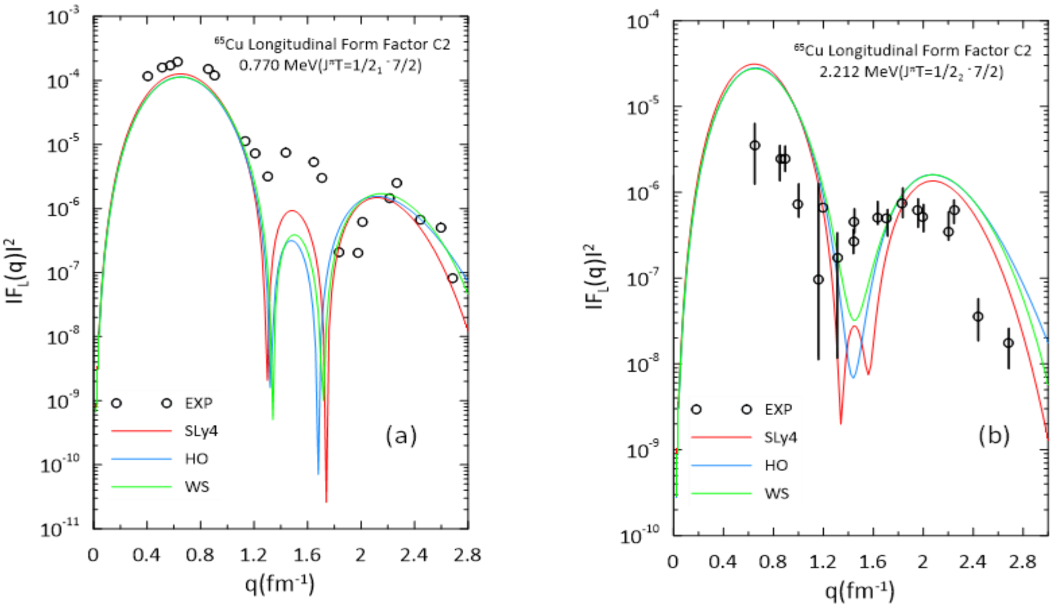

Figure 1: Theoretical longitudinal C2 form factors using HO, WS and SLy4 parameterization for a) $1/2_1$(0.770 MeV), b) $1/2_2$ (2.212 MeV) transitions compared with experimental data [35].

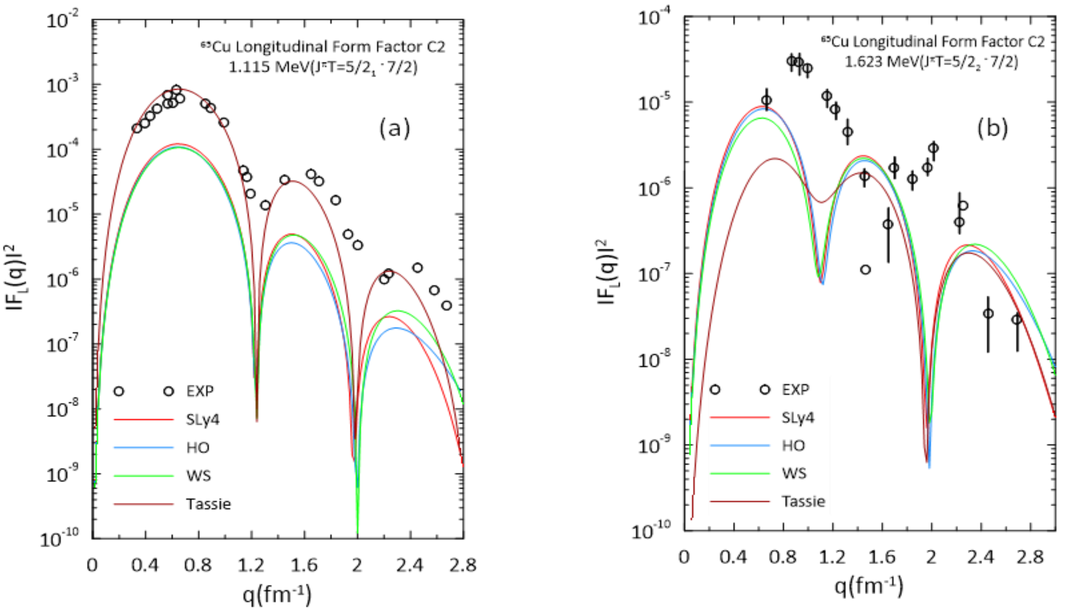

Figure 2: Theoretical longitudinal C2 form factors using HO, WS and SLy4 parameterization for a) 5/2₁(1.115 MeV), b) 5/2₂ (1.623 MeV) transitions compared with experimental data [35].

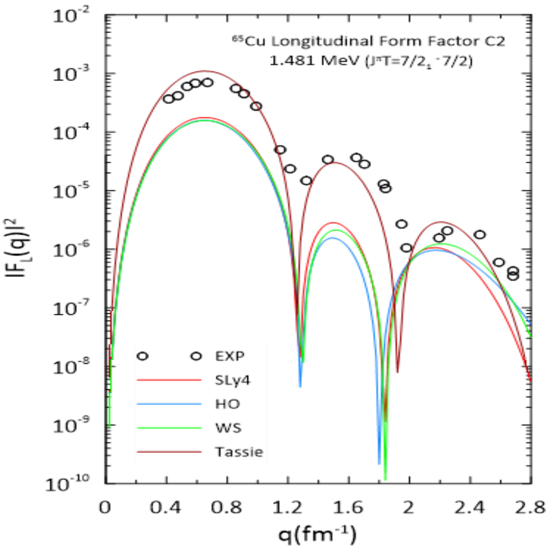

Figure 3: Theoretical longitudinal C2 form factors using HO, WS and SLy4 parameterization for 7/2₁(1.481 MeV) transitions compared with experimental data [35].

3.1.2 Longitudinal C4 form factors

Fig.4 depicts the calculated C4 form factors for the states $5/2_3$ and Fig. 5 for the $7/2_2$, $7/2_3$, and $7/2_4$, compared with experimental data from Erler et al. [35]. In Fig. 4, the C4 form factor for the $5/2_3$ state (2.593 MeV) is well estimated by HO, WS and SLy4 parameterization, while the Tassie model shows some deviations. the deviations are clearly visible at the extreme values, indicating that this model may not account for certain physical effects, such as nuclear deformations or pairing effects. .Fig. (5a) and (5b) present the C4 form factors calculated using the Tassie model for the $7/2_2$ state (2.094 MeV) and $7/2_3$ state (2.278 MeV), which show good agreement with the experimental data. There were two diffraction maxima and one diffraction minimum in the experimental data, but the Tassie model predicted three diffraction maxima and two diffraction minima, which does not fully match the experimental data. In Fig. (5c), the

Tassie model underestimated the first diffraction maximum for the $7/2_4$ state (2.643 MeV) and did not accurately represent the second maximum.

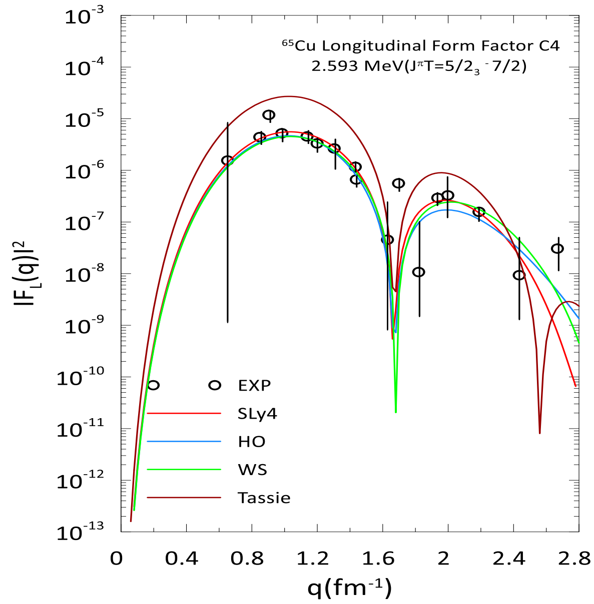

Figure 4: Theoretical longitudinal C4 form factors using HO, WS and SLy4 parameterization for $5/2_3$(2.593 MeV) transitions compared with experimental data [35].

3.1.3 Transverse E2 Form Factors

Fig. (6a) displays the theoretically calculated E2 form factors from (SLy4, HO, and WS) for the $1/2_1$ state (0.771 MeV), which were compared with experimental data that showed significant scatter and high error bars near the first maximum. The theoretical results fell within the error bars at the first maximum and reproduced the experimental data up to q=1.6 fm^{-1} in the second maximum. Fig. (6b) presents the calculated E2 form factor for the $1/2_2$ state (2.212 MeV), compared with the experimental data from the work of Erler et al. [35], which were scattered and had large error bars, making the diffraction maxima and minima less distinct. The theoretical calculations predicted two maxima and one minimum. The E2 transverse form factors for the $5/2_1$ and $5/2_2$ states (1.115 MeV, 1.623 MeV) are shown in Figs. (7a) and (7b), respectively. The results from the three potentials and Tassie models failed to accurately reproduce the experimental data for the transverse form factor of the $7/2_1$ state (1.482 MeV), as represented in Fig. 8.

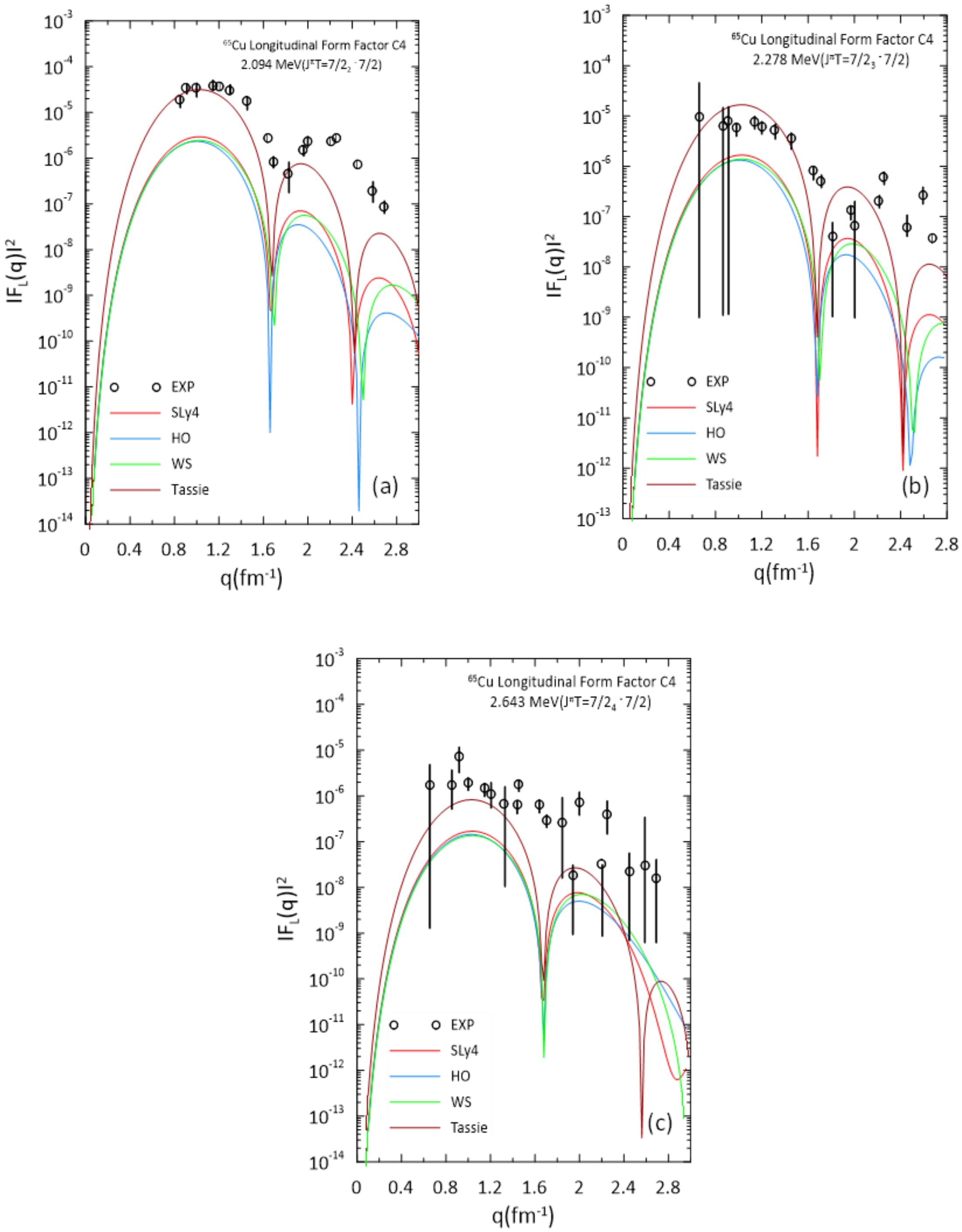

Figure 5: Theoretical longitudinal C4 form factors using HO, WS and SLy4 parameterization for a) $7/2_2$(2.094 MeV), b) $7/2_3$(2.278 MeV), and c) $7/2_4$(2.643 MeV) transitions compared with experimental data [35].

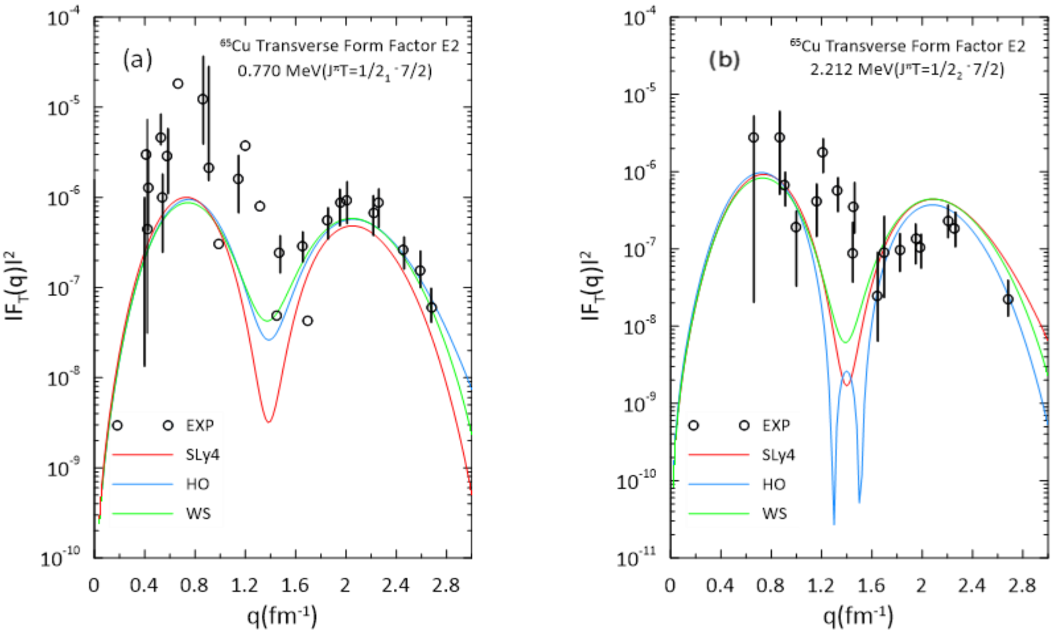

Figure 6: Theoretical transverse E2 form factors HO, WS and SLy4 parameterization for a) $1/2_1$(0.770 MeV), b) $1/2_2$ (2.212 MeV) transitions compared with experimental data [35].

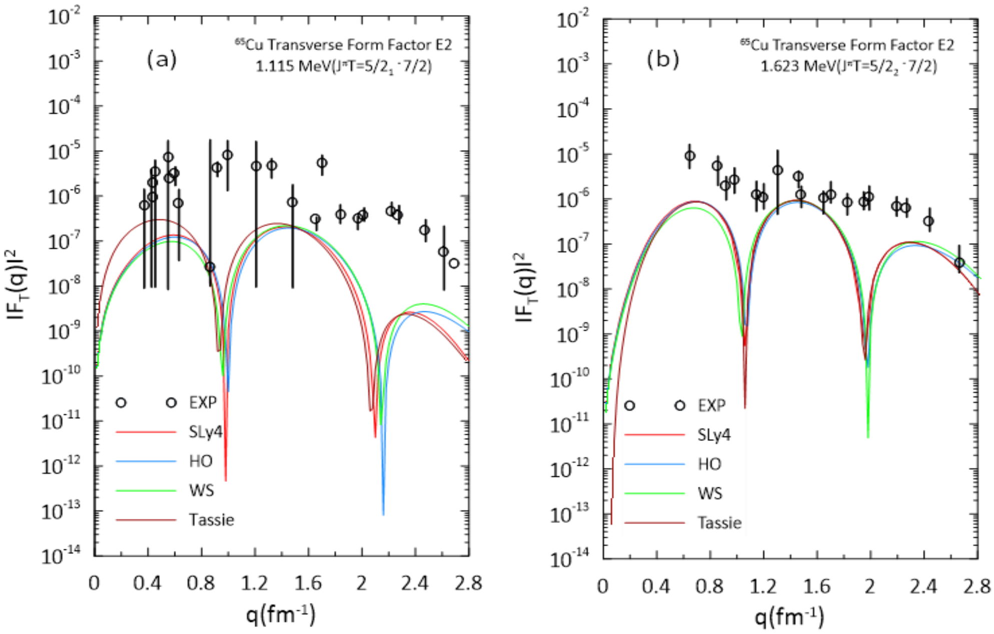

Figure 7: Theoretical transverse E2 form factors HO, WS and SLy4 parameterization for a) $5/2_1$(1.115 MeV), b) $5/2_2$ (1.623 MeV) transitions compared with experimental data [35].

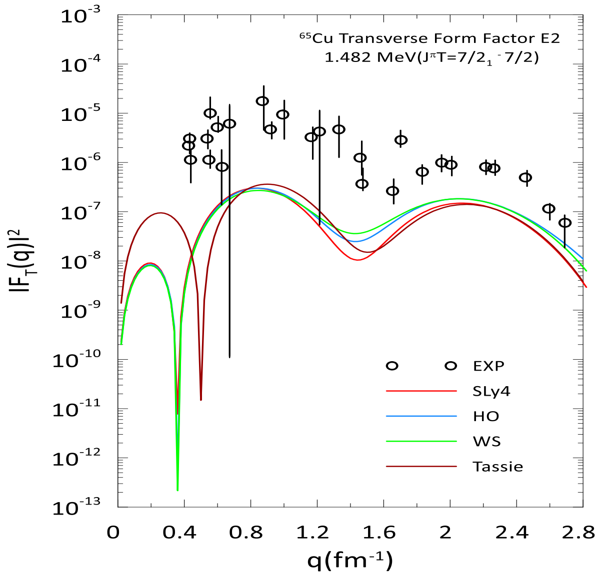

Figure 8: Theoretical transverse E2 form factors HO, WS and SLy4 parameterization for $7/2_1$(1.481 MeV) transitions compared with experimental data [35].

3.1.4. Transverse E4 form factors

The calculated E4 form factors for the state $5/2_3$ is depicted in Fig. 9, and for the states $7/2_2$, $7/2_3$, $7/2_4$ in Fig. 10. For the $5/2_3$ state (2.593 MeV), the experimental data were well-labelled throughout all momentum transfer regions q. The calculations using the three potentials and Tassie model revealed three diffraction maxima, with the lowest peak located in the midst of the diffraction minima. In all momentum transfer locations, the computed E4 form factors for the $7/2_2$ state (2.094 MeV) were lower than the experimental data (Figure 10a). The anticipated E4 form factors computed using the three potentials and Tassie model were similar; the experimental data in both Figs. (10b) and (10c) have significant error bars for the $7/2_3$ (2.278 MeV) and $7/2_4$ (2.643 MeV) states, respectively. the transverse E4 form factor for the state with two diffraction maxima underestimated the measured data and falls within the high error bars. When calculating the state's transverse E4 form factor, the Tassie and three potential models were almost indistinguishable; all four exhibited two diffraction maxima.

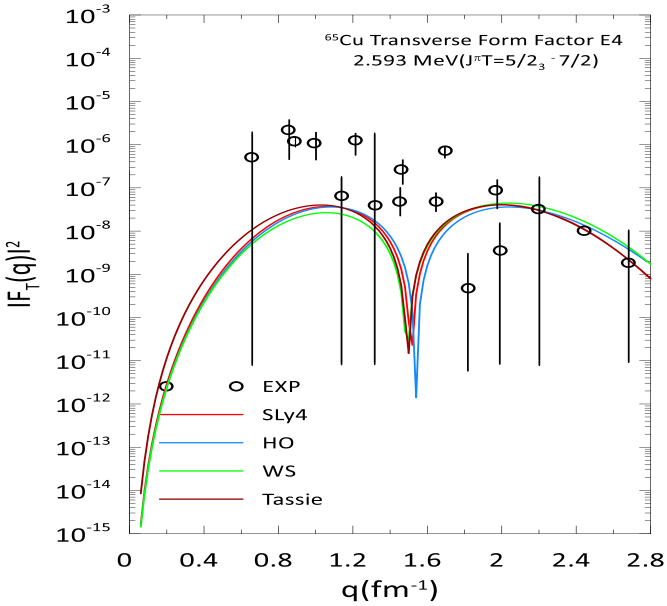

Figure 9: Theoretical transverse E4 form factors HO, WS and SLy4 parameterization for $5/2_3$(2.593 MeV) transitions compared with experimental data [35].

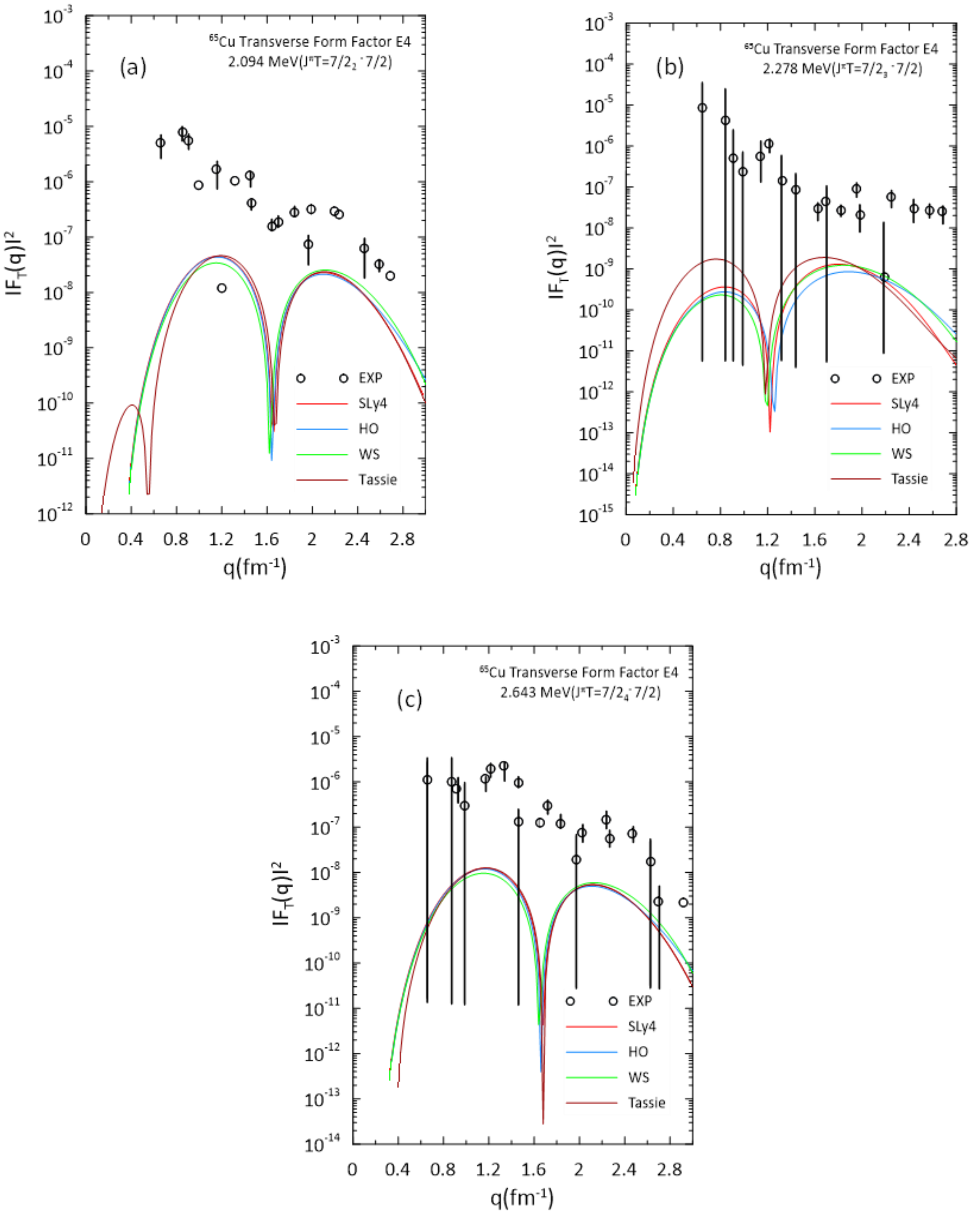

Figure 10: Theoretical transverse E4 form factors HO, WS and SLy4 parameterization for a) $7/2_2$(2.094 MeV), b) $7/2_3$(2.278 MeV), and c) $7/2_4$(2.643 MeV) transitions compared with experimental data [35].

3.2 The Excitation Energies

The established levels of ^{65}Cu (Z=29, N=36) were investigated by the shell model with ^{40}Ca inert core. The calculations adopted the NuShellX code with the *jj44* model space and the jun45 effective interaction [24]. The model space consists of nine protons and sixteen neutrons in orbits ($1f_{7/2}$, $2p_{3/2}$, $2p_{1/2}$, and $1f_{5/2}$). The present results were compared with the experimental data [34], as shown in Fig. 11. The calculations of excitation energies are shown in Table 1.

It was shown that the *fp*-shell model gave an exact theoretical calculation of the excitation energies that agrees with experimental values. Therefore, the *fp*-shell model is considered one of the suitable models for studying the properties of heavy nuclei.

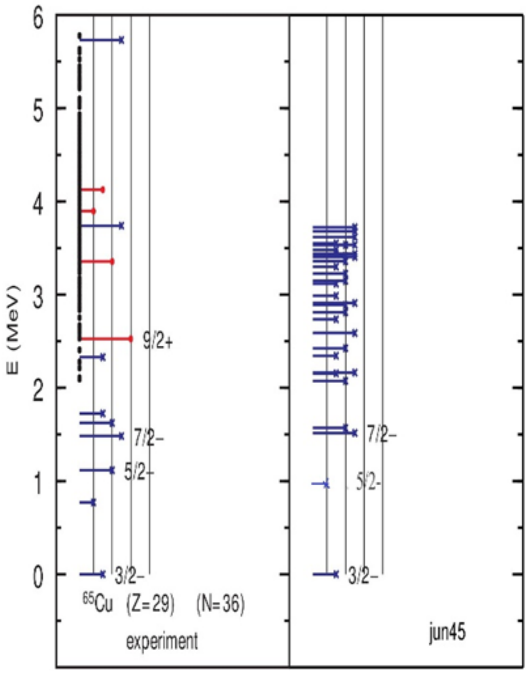

Figure 11: Comparison of excitation energy parts of the experimental ^{65}Cu level schemes with shell model calculations jun45 interaction.

Table1: The results of excitation energies compared with the experiments data [34].

Nucleus $_{29}$Cu A, N	J^{π} T	E_X (Mev)	
		CAL	**EXP**
65 , 36	$1/2_1^- 7/2$	0.931	0.770
	$5/2_1^- 7/2$	1.569	1.115
	$7/2_1^- 7/2$	1.516	1.481
	$5/2_2^- 7/2$	2.074	1.623
	$7/2_2^- 7/2$	2.164	2.094
	$5/2_3^- 7/2$	2.424	2.593
	$1/2_2^- 7/2$	2.259	2.212
	$7/2_3^- 7/2$	2.588	2.278
	$7/2_4^- 7/2$	2.910	2.643

3.3 Quadrupole Deformation

Potential energy curves PEC$_S$ were considered as a function of the β_2 with method HF + BCS based on Skyrme interaction (SLy5) [35]. The shape of the selected ^{65}Cu nuclei was investigated. The left panel illustrates the β_2 parameter for ^{65}Cu as a function of energy. In the right panels, nuclear density calculations for two de^{65}Cu formed shapes labeled as a (upper panel) and b (lower panel) are displayed for neutrons (on the left) and protons (on the right).

In the ^{65}Cu, proton density has the maximum in the center due to the strong nuclear force that overcomes their electric repulsion (Coulomb energy), allowing them to stay close together. Neutrons, being electrically neutral, are unaffected by Coulomb repulsion, but their distribution is less dense at the center to achieve balance and stability in the nucleus based on their interactions with protons, as shown in Fig. 12. The PECs curves for ^{65}Cu have two minima forming a coexistence of oblate and prolate deformations located at β_2 = -0.15 and β_2 = 0.15. These two minima are separated at the potential energy curves equal to -559 MeV and -558.5, respectively.

The deformations at the minimum of energy (at points a and b) have the same value, β_2= 0.151, due to the symmetry in the energy distribution of the nucleus around the symmetry axis. This symmetry leads to a balanced deformation at this particular value, meaning that the nucleus exhibits the same stability at these deformation values, achieving the minimum energy in both cases.

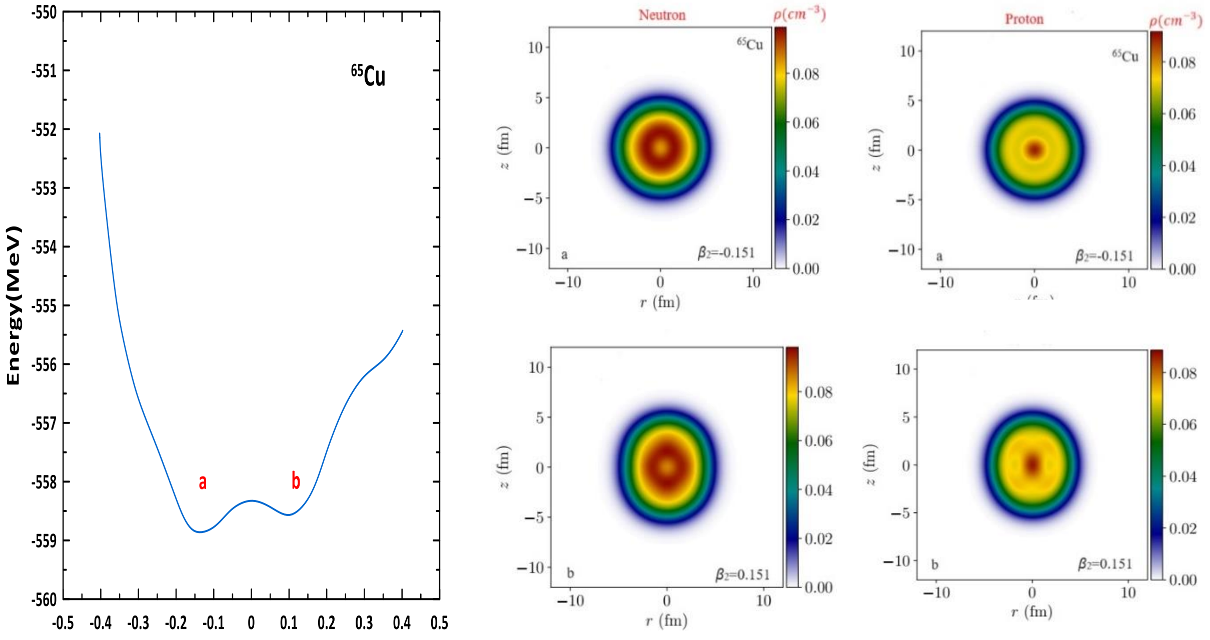

Figure 12: The potential energy curve (PEC$_S$) of ^{65}Cu is shown as a function of β_2 in the left panel, with two deformed shape, marked a (upper panel) and b (lower panel), for neutron (left) and proton (right).

4. Conclusions

Nuclear deformation was studied for ^{65}Cu isotope within the *fp*-shell. The quantitative agreement was satisfying, with C2 form factor estimates using SLy4, HO, WS, and the Tassie model closely matching experimental data. The Tassie model offered better agreement with experimental results, particularly at the first maximum. The C2 and E2 form factors for the excited $1/2_1$ state in Cu isotope, calculated using SLy4, HO, and WS potentials, showed good agreement with experimental data. However, the calculations underestimated the measured data for the excited $1/2_2$ state. The C2 and E2 form factors for the excited $5/2_1$ and $5/2_2$, $7/2^-_1$ states in Cu isotope, calculated using the Tassie model, showed enhancements at the first, second, and third maxima, which aligned with experimental data. The C4 form factors for the $5/2_3$ state in the Cu isotope were well estimated using SLy4, HO, and WS potentials. The calculations for the $7/2_2$, $7/2_3$ and $7/2_4$ states, using the Tassie model, agreed with experimental data. The experimental data were represented within error bars by the virtually identical anticipated E4 form factors for the $7/2_2$, $7/2_3$, $7/2_4$ states in the Cu isotope, using the Tassie model and the three potentials. While the experimental data were overestimated by the transverse E4 form factor calculations for states with two diffraction maxima, the error bars were nevertheless large enough to be considered acceptable.

Conflict of Interest

The author(s) declare that there is no conflict of interest.

References

1. M. Dufour and A. P. Zuker, Phys. Rev. **C 54**, 1641 (1996). https://doi.org/10.1103/PhysRevC.54.1641.
2. A. Bohr and B. R. Mottelson, *Nuclear Structure Benjamin* (New York 1969).
3. S. R. Johnson, R. V. F. Janssens, U. Friman-Gayer, B. A. Brown, B. P. Crider, S. W. Finch, Krishichayan, D. R. Little, S. Mukhopadhyay, E. E. Peters, A. P. D. Ramirez, J. A. Silano, A. P. Tonchev, W. Tornow, and S. W. Yates, Phys. Rev. C **108**, 024315 (2023). https://doi.org/10.1103/PhysRevC.108.024315.
4. L. A. Mahmood and G. N. Flaiyh, Iraqi J. Phys. **62**, 1901 (2021). https://doi.org/10.24996/ijs.2021.62.6.16.
5. B. A. Brown, and B. H. Wildenthal, Ann. Rev. Nucl. Part. Sci. **38**, 29 (1988). https://doi.org/10.1146/annurev.ns.38.120188.000333
6. G. Le Anh, B. Minh Loc, P. Papakonstantinou, and N. Auerbach, Phys. Rev. C **109**, 024313 (2024). https://doi.org/10.1103/PhysRevC.109.024313.
7. Y. M. Xing, Y. F. Luo, K. H. Li, Y. H. Zhang, J. G. Li, M. Wang, Yu. A. Litvinov, K. Blaum, X. L. Yan, T. Liao, M. Zhang, and X. L. Zhou, Phys. Rev. C 111, 024313 (2025). https://doi.org/10.1103/PhysRevC.111.024313.
8. L. A. Mahmood and G. N. Flaiyh, Iraqi J. Phys. **19**, 82 (2021). https://doi.org/10.30723/ijp.19.49.82-93.
9. A. H. Taqi and E. G. Khidher, Pramana-J. Phys. **93**, 60 (2019). https://doi.org/10.1063/5.0093384.
10. A. Ait Ben Mennana, Y. EL Bassem, and M. Oulne, Physica Scripta, **95**, 6 (2020). https://doi.org/10.1088/1402-4896/ab73d8.
11. A. Ait Ben Mennana, Y. EL Bassem, and M. Oulne, Physica Scripta, **95**, 6 (2020). https://doi.org/10.1088/1402-4896/ab73d8.
12. E. Caurier, P. Navratil, W. E. Ormand, and J. P. Vary, Phys. Rev. C **66**, 024314 (2002). https://doi.org/10.1103/PhysRevC.66.024314.
13. R. B. Gajdics, J. J. Tomán, H. Zapolsky, Z. Erdélyi, and G. Demange, J. Appl. Phys. **126**, 065106 (2019). https://doi.org/10.1063/1.5099676.
14. S. J. Ahmad, K. S. Jassim, and F. A. Majeed, J. Adv. Res. Dyn. Control Syst. **12**, 200 (2020). https://doi.org/10.5373/JARDCS/V12I5/20201705.
15. J. Williams, G. C. Ball, A. Chester, T. Domingo, A. B. Garnsworthy, G. Hackman, J. Henderson, R. Henderson, R. Krücken, Anil Kumar, K. D. Launey, J. Measures, O. Paetkau, J. Park, G. H. Sargsyan, J. Smallcombe, P. C. Srivastava, K. Starosta, C. E. Svensson, K. Whitmore, and M. Williams, Phys. Rev. C **100**, 014322 (2019). https://doi.org/10.1103/PhysRevC.100.014322.
16. A. Otsuka, A. Gade, O. Sorlin, T. Suzuki, and Y. Utsuno, Rev. Mod. Phys. **92**, 015002 (2020). https://doi.org/10.1103/RevModPhys.92.015002.
17. P. G. Reinhard, B. Schuetrumpf, and J. A. Maruhn, Comput. Phys. Commun. **258**, 107603 (2021). https://doi.org/10.17632/776b7txmhv.
18. J. Dobaczewski, W. Nazarewicz, T. R. Werner, J. F. Berger, C. R. Chinn, and J. Decharge, Phys. Rev. **C 53**, 2809 (1996).
19. J. Dobaczewski, M. V. Stoitsov, and W. Nazarewicz, arXiv: Nucl-th. 0404077V1 (2004). https://doi.org/10.1063/1.1805914.
20. R. A. Radhi and A. A. Alzubadi, Few-Body Syst. **60**, 57 (2019). https://doi.org/10.1007/s00601-019-1524-x.
21. A. H. Taqi and P. F. Mahmood, Nucl. Phys. **A** **983**, 103 (2019). https://doi.org/10.1016/j.nuclphysa.2019.01.001.
22. M. Honma, T. Otsuka, T. Mizusaki, and M. Hjorth-Jensen, Phys. Rev. C **80**, 064323 (2009). https://doi.org/10.1103/PhysRevC.80.064323.
23. B. A. Brown and W. D. M. Rae, Nucl. Data Sheets **120**, 115 (2014). https://doi.org/10.1016/j.nds.2014.07.022.
24. R. A. Radhi, A. A. Alzubadi, and A. H. Ali, Phys. Rev. C **97**, 064312 (2018). https://doi.org/10.1103/PhysRevC.97.064312.
25. A. A. Alzubadi, Indian J. Phys. **89**, 619 (2015). DOI: https://doi.org/10.1007/s12648-014-0614-3.
26. T. de Forest and J. D. Walecka, Adv. Phys. **15**, 1 (1966). https://doi.org/10.1080/00018736600101254.
27. B. A. Brown, S. E. Massen, P. E. Hodgson, and J. D. Walecka, Phys. Rev. **C 32**, 1127 (1985).
28. A. A. Alzubadi and R. A. Allawi, Indian J. Phys. **96**, 1205 (2022). https://doi.org/10.1007/s12648-021-02052-x.
29. H. Horie and K. Ogawa, Prog. Theor. Phys. **46**, 439 (1971).

30. P. G. Reinhard, B. Schuetrumpf, and J. A. Maruhn, Comput. Phys. Commun. **258**, 107603 (2021). https://doi.org/10.1016/j.cpc.2020.107603.
31. A. A. Alzubadi and R. S. Obaid, Indian J. Phys. **93**, 1 (2019). https://doi.org/ 10.1007/s12648-018-1269-2.
32. H. Ogawa, K. Asahi, K. Sakai, T. Suzuki, H. Izumi, H. Miyoshi, M. Nagakura, K. Yogo, A. Goto, T. Suga, T. Honda, H. Ueno, Y. X. Watanabe, K. Yoneda, A. Yoshimi, N. Fukuda, Y. Kobayashi, A. Yoshida, T. Kubo, M. Ishihara, N. Imai, N. Aoi, W.-D. Schmidt-Ott, G. Neyens, and S. Teughels, Phys. Rev. C **67**, 064308 (2003). https://doi.org/10.1103/PhysRevC.67.064308.
33. L. Tassie, Aust. J. Phys. **9**, 407 (1956).
34. Live Chart of Nuclides, nuclear structure and decay data, https://www-nds.iaea.org.
35. J. Erler, P. Klüpfel, and P. G. Reinhard, J. Phys. G **38**, 33101 (2011). https://doi.org/10.15407/jnpae2020.01.038.

التحقيق في التركيب النووي للنحاس-65 باستخدام نموذج القشرة ونهج هارتري-فوك

رويدة طارق مهدي[1] وعلي عبد اللطيف الزبيدي[2]

[1] قسم الفيزياء، كلية العلوم للبنات ، جامعة بغداد، بغداد، العراق

[2] قسم الفيزياء، كلية العلوم، جامعة بغداد، بغداد، العراق

الخلاصة

تتناول هذه الدراسة خصائص التشوه النووي لنظير ^{65}Cu باستخدام حسابات نموذج القشرة جنبًا إلى جنب مع تقريب هارتري-فوك، وذلك ضمن إطار مساحة نموذج *fp*-shell. تم إجراء تحليل مفصل لاستطارة الإلكترونات غير المرن، مع التركيز على كل من معاملات الشكل الطولية والعرضية، بالإضافة إلى حساب طاقات الإثارة. وقد تم تنفيذ هذه الحسابات باستخدام نموذج القشرة، مع دمج عناصر من مصفوفة كثافة الانتقال أحادي الجسم، والاستفادة من المساحة الكاملة لنموذج *fp*-shell لتسهيل تفاعلJUN45. تم تطبيق دوال موجية نظرية متعددة، بما في ذلك دالة المتذبذب التوافقي (HO)، ودالة هارتري- فوك سكيرم (SLy4)، وجهد وود ساكسون (WS)، وتمت مقارنة نتائجها بدقة مع البيانات التجريبية .علاوة على ذلك، تم استكشاف أسطح الطاقة الكامنة كدالة لمعاملات التشوه الرباعي من خلال معلمات SLy5 ضمن مقاربة هارتري-فوك. ومن الجدير بالذكر أن حسابات نموذج القشرة تم تنفيذها باستخدام برنامج NushellX@MSU دون فرض أي قيود على مساحة النموذج، مما أتاح فهمًا شاملًا وغير مقيد لديناميكيات البنية النووية لنظير ^{65}Cu.

الكلمات المفتاحيه: نموذج قشرة -fp، جهد سكيرم هارتري -فوك، التشوه رباعي القطب، عوامل التشكل، طاقة التهيج .